2011-12-01

Electron screening and disorder-induced heating in ultracold neutral plasmas

Mary Elizabeth Lyon

Brigham Young University - Provo

Electron screening and disorder-induced heating in ultracold neutral plasmas

Mary E. Lyon

A thesis submitted to the faculty of
Brigham Young University
in partial fulfillment of the requirements for the degree of

Master of Science

Scott D. Bergeson, Chair
Justin B. Peatross
Michael J. Ware

Department of Physics and Astronomy

Brigham Young University

December 2011

ABSTRACT

Electron screening and disorder-induced heating in ultracold neutral plasmas

Mary E. Lyon
Department of Physics and Astronomy
Master of Science

Disorder-induced heating (DIH) is a nonequilibrium, ultrafast relaxation process that occurs when laser-cooled atoms are photoionized to make an ultracold plasma. Its effects dominate the ion motion during the first 100 ns of the plasma evolution. Using tools of atomic physics we study DIH with ns time resolution for different plasma densities and temperatures. By changing the frequency of the laser beam we use to probe the ions, we map out the time evolution of the velocity distribution. We can compare this to a fluorescence simulation in order to more clearly determine the relationship between the fluorescence signal and the velocity distribution. In this study we observe and characterize effects due to electron screening on the ions during the equilibration process.

ACKNOWLEDGMENTS

First and foremost I want to offer my sincerest gratitude to Dr. Scott Bergeson, for giving me the opportunity to work in his lab and for his knowledge, guidance, and patience over the past several months. As his student I have not only learned much from his extensive knowledge of physics, but also from the example he sets of excellence, diligence, and integrity in both the personal and professional spheres of his life. I extend this gratitude to the entire Brigham Young University physics department, not only for the wonderful education I have received here but also for the tremendous support and encouragement that I have felt.

I would also like to acknowledge Daniel Thrasher; the time he spent taking data and helping me around the lab made my life easier. I am also grateful for the friendship and support of many others in the physics department and in my personal life. Though they are too numerous to mention by name, I hope they know how much I value them and all that they have done for me.

Last, but never least, I want to express my love and thanks to my family: my parents, Stephen and Gail Lyon; and my siblings, Catherine, Dean, Thomas, and their families. In particular I want to acknowledge and thank my parents, for their constant and consistent love and support, for encouraging me to always ask questions, and for never letting me settle for anything less than my best.

Ultimately, it is to God that I owe my greatest thanks. The miracle of His all-encompassing love is what has sustained me through my efforts. All that I have done and all that I hope to accomplish in the future is only possible through Him and through His Son. I dedicate this work to Them, and will ever seek to put forth only my best efforts, that I might with confidence say that all that I have done has been in Their name and for Their glory.

Contents

List of Figures

Chapter 1

Introduction

Studies of ultracold plasmas are motivated in part by the insight they can provide into similar plasma systems. Due to their large electrical potential energies and comparatively small kinetic energies, ultracold plasmas fall into a regime of plasma systems which are called "strongly coupled." Other strongly coupled plasmas include laser-produced fusion plasmas [1], laser-cooled ion crystals [2], dusty plasmas [3], and a variety of astrophysical systems [4]. Experiments with ultracold plasmas allow us to probe strongly coupled Coulomb systems under a wide range of tunable initial conditions using a table-top apparatus and optical detection techniques. This is because plasma evolution occurs on the time scale of the inverse plasma frequency ω_p^{-1} where the ion plasma frequency is $\omega_p = (ne^2/m_i\varepsilon_0)^{1/2}$ [5–8], and n is the density, e is the fundamental charge, m_i is the ion mass, and ε_0 is the permittivity of free space. For high-density plasmas, this time scale is on the order of femto- or attoseconds. The relatively less dense ultracold plasmas evolve on the nanosecond time scale, which makes it possible to study the plasma characteristics and evolution directly using commonly employed techniques of atomic physics.

Strong coupling is characterized by the ratio Γ of the electrical potential energy to the kinetic

energy

$$\Gamma = \frac{e^2}{4\pi\varepsilon_0 a_{\mathrm{ws}}} \frac{1}{k_{\mathrm{B}} T_{\mathrm{i}}}. \tag{1.1}$$

This ratio is called the strong coupling parameter, where $a_{\mathrm{ws}} \equiv (3/4\pi n)^{1/3}$ is the Wigner-Seitz radius or the average distance between ions, k_{B} is Boltzman's constant, and T_{i} is the ion temperature. Initially this strong coupling parameter is large in ultracold plasmas because the ions retain the low temperature of the laser-cooled atoms, which are at about 1 mK. However the equilibrium strong coupling is limited by the relaxation of the ions due to nearest-neighbor interactions [5, 9–12]. Ultracold plasmas are generally created by photoionizing atoms in a magneto-optical trap (MOT) [13–17]. When the plasma is created, the random distribution of atoms in the MOT gives rise to spatially uncorrelated ions. Even though the ions have essentially zero kinetic energy, they have a great deal of electrical potential energy. The ions move to minimize the excess electrical potential energy, increasing their kinetic energy. This heating mechanism is called "disorder-induced heating" (DIH) [5, 10–12, 18] and it raises the ion temperature to the correlation temperature

$$T_c = \frac{2}{3} \frac{e^2}{4\pi\varepsilon_0 a_{\mathrm{ws}} k_{\mathrm{B}}}. \tag{1.2}$$

On the timescale of the inverse plasma frequency ω_p^{-1}, motion of the ions after the plasma is created is dominated by nearest-neighbor interactions. The ions oscillate in a local potential that is determined by neighboring ions and free electrons as they seek to minimize their excess electrical potential energy.

The goal of this project is to understand the time scale over which DIH occurs and the influence of electron screening on the DIH process. We map out the velocity distribution of the ions as the plasma evolves for a range of initial electron temperatures and plasma densities. Experimental data is compared with simulations of the plasma evolution, which help us better understand the relationship between DIH and the time evolving velocity distribution. By exploring the plasma dynamics during this DIH phase we hope to find a way to minimize its effects and increase the

strong coupling parameter in our ultracold plasmas.

1.1 Plasma characteristics

Plasmas comprise the vast majority of the known universe. These plasmas exist over a wide range of temperatures T_e and densities n. In the low-temperature, low-density regime that ultracold plasmas occupy, we are concerned with initial electron temperatures as low as 0.5 K and densities on the order of 10^{10} ions per cm^3, or 10^{16} per m^3. The initial density profile of ultracold plasmas typically reflect the nearly Gaussian densities of the trapped atoms in the MOT, which density is given by

$$n(r) = n_0 \exp[-r^2/2w^2] \tag{1.3}$$

where r is the plasma radius and w is the Gaussian width of the plasma.

After the atoms in the MOT are ionized, the resulting plasma is not confined. As the plasma expands, the density changes. The time-dependent density profile is given by

$$n(r,t) = n_0 \exp[-r^2/2w^2(t)][w_0/w(t)]^3, \tag{1.4}$$

where n_0 is the peak density in the plasma, w_0 is the initial plasma size, and $w(t) = \sqrt{w_0^2 - v_{exp}t^2}$ is the Gaussian radius. The expansion velocity $v_{exp} \equiv \sqrt{k_B T_e/m_i}$ depends on the initial electron temperature T_e, which is controlled by the wavelength of the ionizing laser [14]. It was shown in Ref. [19] and Ref. [20] that if the initial electron strong coupling parameter is not too high ($\Gamma_e \ll 1$), and the plasma density is sufficiently low that the expansion velocity is the rate at which the plasma expands radially outward in a self-similar (Gaussian) manner. This expansion is driven by the electron pressure, which is a term used to describe the effect of electrons trying to leave the plasma and exerting a force on the ions as they try to do so. When the plasma is first created, some of the electrons have enough kinetic energy to escape the Coulomb potential of the ions. However, with

the loss of these electrons the Coulomb potential well deepens and traps the remaining electrons, leaving the plasma largely neutral [21].

An important length scale used in plasma physics is the Debye length, $\lambda_D = (k_B T_e \varepsilon_0/ne^2)^{1/2}$. Debye shielding, or electron screening, happens when charges are able to redistribute themselves to screen electric fields and occurs on the length scale of the Debye screening length. When the Debye length is comparable to the distance a_{ws} between ions electron screening reduces the ion-ion potential energy. The influence of electron screening is seen as a slowing of the ion motion during the DIH phase and a reduction of the equilibrium temperature [5].

1.2 Theoretical models

Previous work with ultracold plasma simulations showed that ion motion during the DIH phase appeared to be more or less unchanged with increased electron screening [6]. This past work showed that the nominal ion plasma frequency set the time scale for DIH and that this time scale was essentially unaffected by electron screening. The following sections give the theoretical background for the relationship between electron screening and the ion plasma frequency.

1.2.1 Nearest-neighbor model

One can imagine two ions fixed on the $x-$axis at a distance $\pm a$ from the origin (see Fig. 1.1). If a third ion, a test particle, constrained to move only along the x-axis, is placed a small distance x from the origin and released, it will execute an oscillatory motion. The force on the test particle can be written and expanded for $x \ll a$. The leading non-vanishing term is linear in x, similar to a harmonic oscillator. From this expression we can extract the oscillation frequency.

If the screening length is λ_D, the force on the test particle is

$$F = -\frac{e^2}{2\pi\varepsilon_0 a_{ws}^3}\left(1 + \kappa + \frac{\kappa^2}{2}\right)\exp(-\kappa)\,x, \tag{1.5}$$
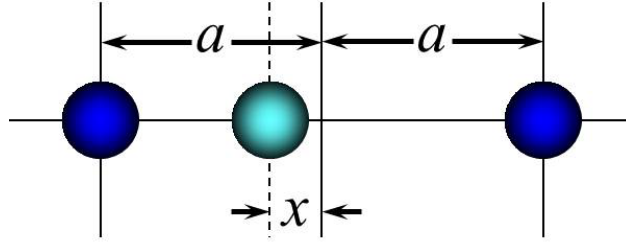
Figure 1.1 A one dimensional representation of the nearest neighbor model. The displaced test particle will oscillate about the origin. If the displacement is much smaller than a, the force on the test particle is linear in x, and can be modeled as a harmonic oscillator.

where e is the ion charge and $\kappa = a_{\mathrm{ws}}/\lambda_{\mathrm{D}}$ is the inverse scaled screening length. This force is linear in x when $x \ll a$. If we recognize this as a simple harmonic oscillator, we can write the ion oscillation frequency as

$$\omega = \omega_p f(\kappa), \tag{1.6}$$

where $f^2(\kappa) = (2/3)(1 + \kappa + \kappa^2/2)\exp(-\kappa)$ and $\omega_p = (ne^2/4\pi\varepsilon_0)^{1/2}$. Expanding this expression to the first non-vanishing correction in κ gives

$$\omega \approx 0.82\omega_p \left(1 - \frac{\kappa^3}{12} \right), \tag{1.7}$$

showing that the oscillation frequency in this overly simple one-dimensional model goes down as κ increases, but that this dependence is very weak.

1.2.2 Molecular dynamic model

A detailed treatment of the initial ion motion in ultracold plasmas is given in Ref. [6]. The early-time evolution of the velocity distribution is described by Eq. (3) in that paper,

$$T(t) = T(0) + (t/\tau_2)^2 + (t/\tau_4)^4 + \cdots, \tag{1.8}$$

where T is the effective ion temperature in units of $e^2/4\pi\varepsilon_0 a_{ws} k_B$ and t is the time in units of the plasma period. If we write the effective ion temperature in SI units as $T = m_i v_{rms}^2/k_B$ and take the initial ion temperature $T(0) = 0$, then this equation can be rewritten as

$$v_{rms}^2 = \left(\frac{e^2}{4\pi\varepsilon_0 m_i a_{ws}}\right)\left(\frac{ne^2}{m_i\varepsilon_0}\right)\left(\frac{t^2}{\tau_2^2}\right),\tag{1.9}$$

where we have kept only the leading term in the series. From the simulation, the parameter $\tau_2 = 3/(33 - 4\kappa + 0.1\kappa^2)^{1/2}$. We solve Eq. (1.9) for v_{rms} and find

$$\begin{aligned}v_{rms} &= 1.1055 a_{ws}\omega_p^2\left(1 - 0.1212\kappa + 0.0030\kappa^2\right)^{1/2}t\\ &\approx 1.1055 a_{ws}\omega_p^2(1 - 0.0606\kappa - 0.0003\kappa^2)t.\end{aligned}\tag{1.10}$$

The inverse scaled screening length scales with electron temperature and density as $\kappa \propto T_e^{-1/2}n_0^{1/6}$. In the context of this thesis, the important result of these two models is that the initial acceleration due to DIH has an extremely weak dependence on κ, meaning that the density dependence of the DIH process is predicted to be extremely weak, since $\kappa \propto n_0^{1/6}$.

The previous work outlined in Sec 4.1 of this thesis and described in detail by us in Ref. [22] indicates that the acceleration of the ions due to DIH depends more strongly on the density and temperature than predicted by these models. The primary objective of the research for this thesis is to verify and better understand the results of this previous study. My contribution includes changes to the experimental setup and the taking and analysis of new data subsequent to our initial publication [22]. This new data was taken for different initial electron temperatures, which correspond to different values of κ, and at different detunings of the laser used to probe the ions. The data was then analyzed to find the rms velocity of the ions as they undergo DIH. We map out the rms velocity distribution in order to see how the motion of the ions changes for different values of κ and to see the effect that electron screening has on the acceleration of the ions during the DIH phase.

Chapter 2

Experimental Setup

2.1 Plasma formation

The process of plasma formation begins in a MOT, where 2×10^7 ^{40}Ca atoms are laser-cooled
and trapped. We then photoionize the trapped calcium using a two-photon ionization process.
We use absorption and fluorescence spectroscopy to make measurements of the plasma. We have
chosen calcium because the energy level transitions required for trapping, ionization, and detection
correspond to laser wavelengths that are readily attainable (see Fig. 2.1). Calcium is an alkaline-
earth metal, which means that it retains one valence electron after ionization. This allows us to use
optical spectroscopy techniques to measure density and temperature. A basic explanation of the
processes of laser cooling and trapping, ionization, and plasma detection will be provided as well
as details regarding our experimental apparatus.

2.1.1 Laser cooling and trapping

Atom trapping in a MOT is a two-fold process that requires individual but closely related mech-
anisms for cooling and trapping atoms. A velocity-dependent force is produced by means of the
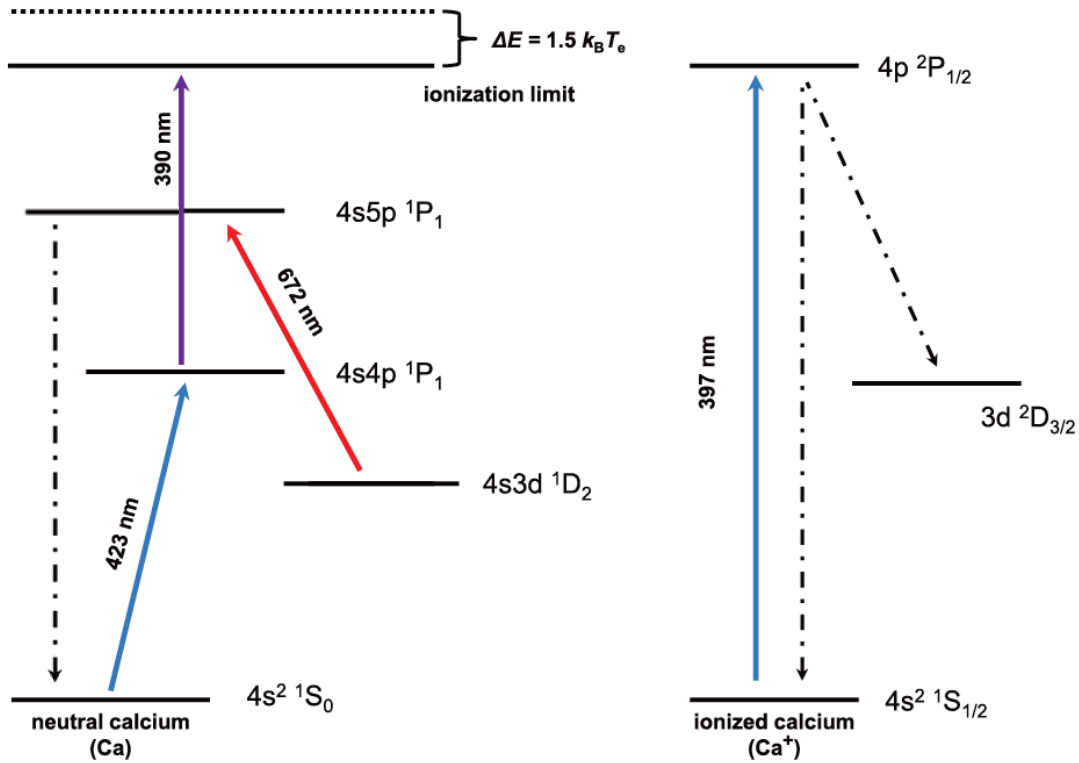
Figure 2.1 Partial energy level diagram for Ca (left) and Ca$^+$ (right). Atoms are cooled and trapped in the MOT using the 423 nm transition. A repump laser at 672 nm pumps atoms that fall into the metastable $4s3d\ ^1D_2$ state back the ground state. The MOT atoms are ionized using a resonant two-step process at 423 and 390 nm. The electron temperature depends on the amount by which the 390 nm laser photon energy exceeds the ionization potential. Spectroscopy of the plasma ions uses the 397 nm resonance transition. Resonantly scattered photons are detected by a fast photomultiplier tube. The Ca$^+$ $^2P_{1/2}$ state ($\tau = 7.2$ ns) has a $\sim 7\%$ decay branch to the $^2D_{3/2}$ dark state.
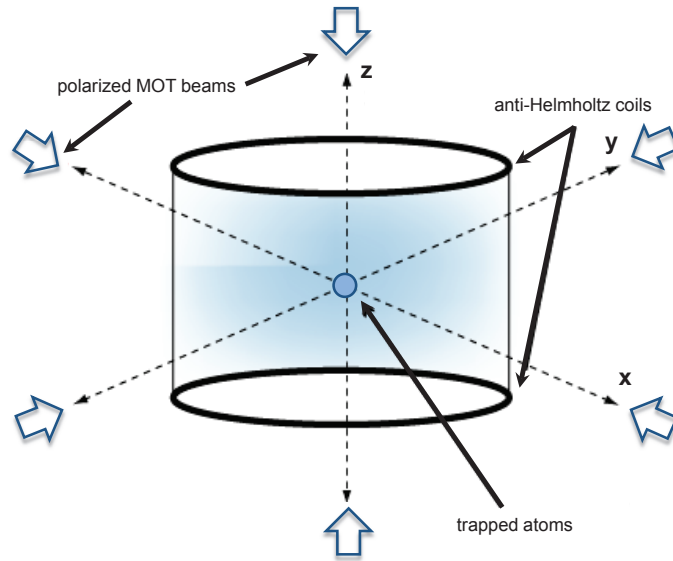
Figure 2.2 Magneto-optical trap (MOT). Six orthogonal beams, tuned to the $4s^2\ ^1S_0 \rightarrow 4s4p\ ^1P_1^o$ transition in calcium at 423 nm, converge at a point at the center of the trap, where the magnetic field produced by the anti-Helmholtz coils is zero. The six beams provide a damping force in all three spatial directions.

Doppler shift. The use of a spatially varying magnetic field produces a position-dependent restoring force via the Zeeman shift. A MOT consists of six orthogonal, counter propagating beams that are slightly detuned below the atomic resonance frequency, as depicted in Fig. 2.2. In our experiment, the trapping laser is tuned one atomic linewidth (approximately 35 MHz) below the $4s^2\ ^1S_0 \rightarrow 4s4p\ ^1P_1^o$ transition in calcium at 423 nm. Atoms moving anti-parallel to the laser beam see the laser Doppler shifted into resonance. The absorption of photons causes the atoms to recoil, due to conservation of momentum, and effectively pushes the atoms back towards the center of the trap.

A pair of coils in an anti-Helmholtz configuration creates a quadrupole magnetic field that is zero at the trap's geometric center and increases linearly in magnitude in the region of the trap's
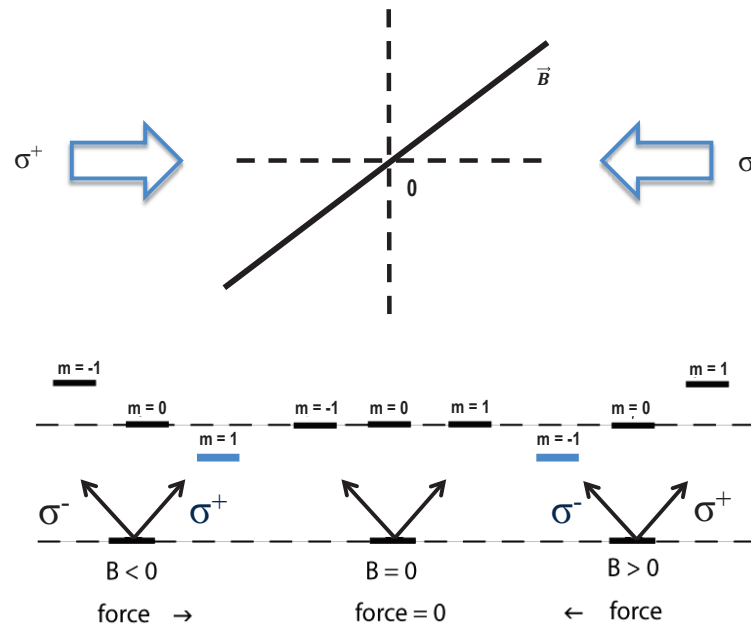
Figure 2.3 A one-dimensional representation of Zeeman shifting and quantum selection rules in a MOT for a two-level atom. To the right of the zero of the magnetic field the magnetic sublevels of the excited state are shifted so that the $m = -1$ state is on resonance with the laser beam. A transition from the ground state to the $m = -1$ excited state is induced by the left circularly polarized photons impinging from the right. The opposite is true for atoms to the left, where the right circularly polarized laser only excites atoms to the $m = +1$ state, which has been shifted by the magnetic field so that it is on resonance with the laser beam. Thus the photon scattering rates are regulated and the result is a position-dependent restoring force that pushes the atoms towards the center of the trap, where the magnetic field equals zero.

center. The magnetic field Zeeman shifts the magnetic sublevels of the $4s4p\ ^1P_1^o$ state. Left and right circularly polarized light is used to regulate the absorption of photons via quantum mechanical selection rules (see Fig. 2.3) The end result is a neutral calcium atom trap that cools the atoms to about 1 mK and confines them to a roughly spherical region less than 1 mm in diameter.

The calcium atoms are produced by a temperature controlled oven that heats bulk calcium into an atomic vapor. The atoms leave the oven through a 1 mm diameter, 10 mm long nozzle, which creates an atomic beam of neutral calcium. A laser beam directed opposite the atomic beam slows

the atoms down and increases the loading rate of the MOT. We detune this "slowing" laser beam several linewidths (about 145 MHz) below the 423 nm atomic resonance. A 672 nm "repump" laser pumps atoms that fall into the metastable $4s3d\ ^1D_2$ state back into the ground state via the highly excited $4s5p\ ^1P_1$ state (see Fig. 2.1). With the slowing laser beam and repump laser this experiment typically achieves peak MOT densities on the order of 10^{10} cm^{-3}.

The 423 nm trapping laser beam is generated by amplifying and frequency doubling an 846 nm diode laser. We use saturated absorption spectroscopy to lock the trapping laser to the appropriate resonance transition.

2.1.2 Plasma creation

Once the calcium atoms are trapped, we photoionize them using a two-photon ionization process. This ionization is achieved using two counter-propagating 3 ns pulse lasers at 423 nm and 390 nm (see Fig. 2.1). These lasers drive the $4s^2\ ^1S_0 \rightarrow 4s4p\ ^1P_1^o$ and the $4s4p\ ^1P_1^o \rightarrow$ **continuum** transitions, respectively. The 390 nm pulse is generated from a tunable dye laser, pumped by a 355 nm pulsed Nd:YAG laser. By adjusting the wavelength of the 390 nm laser (which drives the transition into the continuum), we can vary the initial energy of the electrons in the plasma, because the excess photon energy above the ionization limit is carried away by the electrons. The minimum temperature of electrons in plasmas ionized right at threshold is determined by the 0.5 cm^{-1} bandwidth of the ionizing laser to about 0.5 K.

2.2 Plasma detection and density measurements

A variety of methods have been used to measure ion dynamics in ultracold plasmas. Some of the earliest ultracold plasmas at NIST in Maryland were probed using rf techniques [14]. An rf signal of known frequency is applied to an expanding plasma. When the plasma frequency,

which depends on density, matches the frequency of the rf signal, the plasma electrons begin to oscillate and are ejected from the plasma. These electrons are then measured by a channeltron. Changing the rf frequency and measuring the electron count for different times allows one to map out the average density of the plasma. This technique provides averaged measurements, but has poor temporal resolution and no spatial resolution. Later, other techniques, such as absorption imaging [10] and fluorescence spectroscopy [11], were developed which provided much better temporal and spatial resolution.

2.2.1 Optical absorption

Optical absorption detection uses a probe laser beam tuned to a resonance transition in the ions. The plasma is illuminated by the probe beam, and the laser intensity is measured by a CCD camera with and without the plasma. Absorption of the probe laser beam is given by Beer's Law, $I = I_0 exp[OD]$, where OD is the optical depth. Taking the ratio of the measurements made with the CCD camera allows us to calculate the optical depth. The transmission signal, $T = 1 - A$, is used to calculate the optical depth:

$$
\begin{aligned}
OD(x,y,z) &= -ln[T_{background}/T_{plasma}] \\
&= \alpha(\nu) \int_{-\infty}^{\infty} dz\, n_i(x,y,z), \\
&= \sqrt{2\pi} w_z \alpha(\nu) n_{0i} \exp\left[-\frac{x^2+y^2}{2w^2}\right],
\end{aligned}
\tag{2.1}
$$

where n_{0i} is the peak ion density and $\alpha(\nu)$ is the absorption cross section [10]. Absorption imaging is a significant improvement over the rf techniques used to probe the first ultracold plasmas. It provides information about the spatial resolution and has much better temporal resolution, but is still limited by the time response of the CCD camera to about 25 ns.

2.2.2   Fluorescence spectroscopy

Studies of early plasma dynamics on the nanosecond time scale require even finer temporal resolution. This can be accomplished using fluorescence spectroscopy on the plasma ions. A cw probe laser beam, tuned to the $^2S_{1/2} \rightarrow {}^2P_{1/2}$ transition at 397 nm (see Fig. 2.1), is directed through the plasma and is absorbed. The ions are excited to the $^2P_{1/2}$ state, then emit photons in all directions as they spontaneously decay. Ions can also be optically pumped into the $^2D_{3/2}$ dark state, also shown in Fig. 2.1. The branching fraction into the dark state is about 7%. The intensity of the probe laser beam at the plasma is typically about $s_0 = I/I_{\text{sat}} = 2$. The natural linewidth γ_{N} of the 397 nm transition equals $1/2\pi\tau$ or 22 MHz. Fluorescence at 397 nm is collected using a lens, isolated using an optical band-pass interference filter, detected using a 1-GHz bandwidth photo-multiplier tube (PMT), and recorded using a 1-GHz bandwidth digital oscilloscope.

Fluorescence and absorption spectroscopy are effective detection tools because they are sensitive to ion motion and plasma dynamics through the Doppler shift. Ions at nearly zero velocity scatter photons from a resonant probe laser beam, producing a fluorescence signal. As the ions accelerate, their velocity (or temperature) increases and they are Doppler-shifted out of resonance with the probe beam. Ions that are no longer resonant with the probe beam are less likely to scatter photons, corresponding to a drop in the fluorescence signal. Thus the signal is roughly proportional to the number of ions Doppler shifted into resonance with the probe. The detuning of the probe laser beam depends on the ions' motion due to DIH, the plasma expansion, and the initial detuning of the probe laser from the ion resonance frequency. Changing the initial offset of the probe laser allows us to probe ions of different velocity classes and to subsequently map out the time evolution of the (non-equilibrium) velocity distribution. In our experiment, the 397 nm laser is locked to the ion transition using saturated absorption (rf modulation transfer) spectroscopy. A portion of the 397 nm laser beam is split off and frequency-shifted by an acousto-optic modulator (AOM) before being sent through the plasma. Using an AOM we detune the probe laser beam by -40, -70, -105,

-140, and -200 MHz.

We can take a more detailed approach to understanding the relationship between the fluorescence signal and the ion dynamics if we use a Voigt profile to extract the effective ion temperature. The Voigt profile is a mathematical representation of the absorption cross section per atom. It is the convolution of a Lorentzian (L) and a Gaussian (G) lineshape

$$
\begin{aligned}
V(f') &= \int_{-\infty}^{\infty} L(f-f')G(f)df \\
&= \int_{-\infty}^{\infty} \frac{\gamma/2\pi}{(f-f')^2 + \gamma^2/4} \cdot \frac{1}{\sqrt{2\pi}v} \exp[-f^2/2v^2]df,
\end{aligned}
\tag{2.2}
$$

where f is the frequency of the transition, f' is the detuning from resonance, γ is the natural linewidth of the atom (the FWHM of the Lorentzian line shape), and v is the rms Doppler width. Integrating Eq. (2.2) for $f' = 0$ gives

$$
V(0) = \frac{1}{\sqrt{2\pi}v} \exp\left(\frac{\gamma^2}{8v^2}\right) \text{erfc}\left(\frac{\gamma}{\sqrt{8}v}\right),
\tag{2.3}
$$

where erfc is the complementary error function. Using the Doppler shift we can map the ion velocity onto the frequency by making the substitution $\gamma = v_n/\lambda$ and $v = v_{th}/\lambda$, where v_n is the velocity that corresponds to the Doppler shift equal to the natural linewidth and v_{th} is the rms thermal velocity, $\sqrt{k_B T_i/m_i}$. Making this substitution into Eq. (2.3) gives

$$
V(0) = \frac{\lambda}{\sqrt{2\pi}v_{th}} \exp\left(\frac{v_n^2}{8v_{th}^2}\right) \text{erfc}\left(\frac{v_n}{\sqrt{8}v_{th}}\right).
\tag{2.4}
$$

For calcium $v_n = \gamma\lambda = 8.7$ m/s. In Sec. 4.3 we describe how we fit the fluorescence signal at different detunings to a similar profile to extract the rms velocity width.

2.2.3 Density measurements

The density of the plasma is determined using a variation of the absorption imaging technique described in Sec. 2.2.1. We measure the density of the atoms in the MOT before and after ionization,

and the change in the MOT density gives us the plasma density. A 423 nm probe beam, resonant with the $4s^2 \, {}^1S_0 \rightarrow 4s4p \, {}^1P_1^o$ transition in neutral calcium, is focused through the center of the MOT before and after ionization. The transmitted light is detected using a PMT. The transmission signal is used to calculated the optical depth, which is related to the density by Eq. (2.1). From Beer's Law and Eq. (2.1) we get

$$T = \exp\left[-\alpha(v) \int dz \, n(z)\right] \tag{2.5}$$

for the transmission. The optical depth is

$$-\ln(T) = \alpha(v) \int dz \, n(z). \tag{2.6}$$

For these measurements, the probe laser beam is directed along the z-axis through the geometric center of the plasma and focused at $x = y = 0$, which means that these equations, as well as Eq. (1.1) and Eq. (1.3), depend only on z. Additionally, since we measure the density of the neutral calcium, we can use Eq. (1.3) to find $n(z)$, which does not depend on the plasma expansion. The difference in optical depth is therefore

$$
\begin{aligned}
ln(T_a) - ln(T_b) &= -\alpha(v) \int n_{0a} \exp(-z^2/2w^2)dz \; + \; \alpha(v) \int n_{0b} \exp(-z^2/2w^2)dz \\
&= (n_{0b} - n_{0a})\alpha(v) \int \exp(-z^2/2w^2)dz.
\end{aligned} \tag{2.7}
$$

Measurements are taken before and after ionization, as denoted by the subscripts b and a, respectively. When the plasma is created, the atoms which are ionized no longer interact with the 423 nm probe beam. This accounts for the change in the measured intensity signal, shown in the sample absorption data in Fig. 2.4. Therefore the peak plasma density n_{0i} is equal to the change in the MOT density

$$n_{0i} = n_{0b} - n_{0a} = \frac{ln(T_b/T_a)}{\alpha(v) \int \exp(-z^2/2w^2)dz}. \tag{2.8}$$

With the 423 nm probe beam exactly on resonance, the absorption cross section is $\alpha(0) = 3\lambda^2/2\pi$.
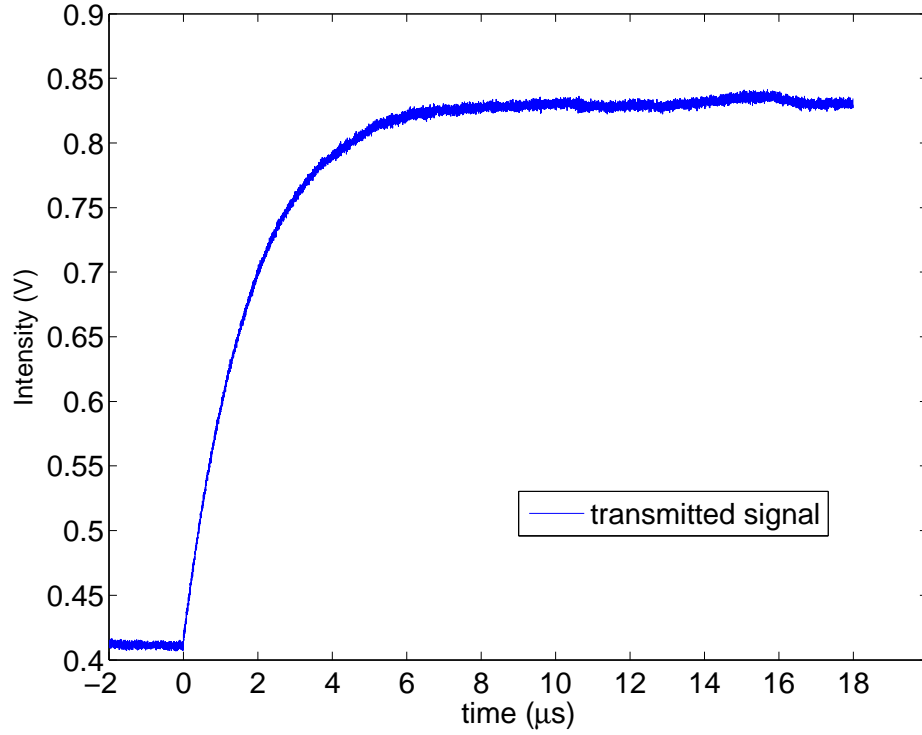
Figure 2.4 Sample absorption data. The transmission of the 423 nm probe laser beam is measured as a function of time.

We can now simplify the denominator of Eq. (2.8) to

$$\alpha(v) \int \exp(-z^2/2w^2)dz = \frac{3\lambda^2 w}{\sqrt{2\pi}}. \tag{2.9}$$

The calculated initial plasma density is therefore

$$n_{0i} = \frac{\sqrt{2\pi} \, ln(T_b/T_a)}{3\lambda^2 w}. \tag{2.10}$$

Chapter 3

Simulation

In order to better understand our experimental results and to test our data analysis, which are described in Chapter 4, we use a computer simulation that integrates the optical Bloch equations to give us a simulated fluorescence signal. The computer simulation allows us to connect our experimental data to information about the plasma evolution that would be difficult to obtain otherwise, such as the velocity distribution and ion temperature at early times. The simulations were carried out by our colleague F. Robicheaux, and are described here for completeness.

3.1   Ion motion and the Yukawa potential

In neutral plasmas, electrons shield ion interactions. If the electron temperature is not too low, the ion-ion potential can be modeled as a Yukawa potential [23]

$$V(r) = \frac{e^2}{4\pi\varepsilon_0} \frac{e^{-r/\lambda_{\mathrm{D}}}}{r}.$$

(3.1)

In the computer simulation we use, ions interact via the Yukawa potential. We assume an isothermal electron distribution, where $\Gamma_e < 1$. Plasma ions are randomly distributed over a cubic cell of approximate dimensions $L = w/10$. The cell dimensions are smaller than the rms size of the

plasma but larger than the Debye screening length. The density is constant across the cell, and we use wrapped boundary conditions to maintain a constant number of ions in the cell. We find the x, y, and z components of the force on each ion due to the screened interactions of all the other ions by taking the gradient of Eq. (3.1). From the calculated force we find the acceleration of each ion. We move the ions in time using a fourth-order Runge-Kutta stepper.

Ions move within the cell and experience a Doppler shift of the probe laser beam frequency, given by

$$\Delta\omega = \frac{2\pi f}{c}v \qquad (3.2)$$

where f is the atomic resonance frequency in the rest frame of the atom, c is the speed of light, and v is the component of the atomic velocity along the direction of the laser beam propagation. Another shift of the probe beam frequency comes from the radial acceleration of the plasma as the plasma expands. At early times, the plasma expansion can be approximated as

$$v_{\text{exp}}(r,t) = r\frac{2k_B T_e}{m_i w}t \qquad (3.3)$$

where r is the radial coordinate and t is the time. This model also assumes an isothermal electron distribution. The temperature of the electrons changes in time due to plasma expansion, evaporation, electron-ion recombination, and electron-Rydberg collisions, however these changes in the electron temperature can be neglected at early enough times. Similarly, at these early times the plasma ions accelerate, but the density profile of the plasma does not change. Thus we can say that this model is valid for early times, when the electron temperature is not too low.

Using the components of the force derived from the Yukawa potential, we calculate the position and velocity of each ion for every time step. Information about the ion velocity, which includes the contribution of the overall plasma expansion, is used to find the ion's frequency shift $\omega = \omega_o - \omega_{laser}$. This detuning is necessary for solving the optical Bloch equations to find the evolution of the Bloch vector and the excited-state fraction, which gives the simulated fluorescence signal.

3.2   Optical Bloch equations

Since the fluorescence signal is proportional to the excited-state fraction, care must be taken to simulate the evolution of the internal state of the ions. This is accomplished by solving the optical Bloch equations at each time step for each ion in the cell. The ions are approximated as two-level atoms dressed by a light field. The Hamiltonian of this system is

$$H = H_{atom} + H_{laser} \tag{3.4}$$

where H_{atom} is the Hamiltonian of the atom and H_{laser} is the Hamiltonian of the light field. Using the rotating wave approximation (RWA) we can write the total Hamiltonian as

$$H = \hbar \omega \sigma_- \sigma_+ + \frac{\hbar \Omega}{2}(\sigma_- + \sigma_+), \tag{3.5}$$

where ω is the detuning, Ω is the Rabi frequency, and the raising and lowering matrices are

$$\sigma_+ = \begin{pmatrix} 0 & 1 \\ 0 & 0 \end{pmatrix} \quad \sigma_- = \begin{pmatrix} 0 & 0 \\ 1 & 0 \end{pmatrix}. \tag{3.6}$$

Written in terms of matrices, the Hamiltonian is

$$H = \begin{pmatrix} 0 & 0 \\ 0 & -\hbar \omega \end{pmatrix} + \begin{pmatrix} 0 & \frac{\hbar \omega}{2} \\ \frac{\hbar \omega}{2} & 0 \end{pmatrix}. \tag{3.7}$$

The equation for the density matrix is given by the Liouville-Bloch equation with decay, found in Eq. (1) of Ref. [24]

$$\dot{\rho} = -\frac{i}{\hbar}[H(t), \rho] - \Gamma(t)\rho. \tag{3.8}$$

The density matrix ρ and its time derivative $\dot{\rho}$ are

$$\rho = \begin{pmatrix} \rho_{ee} & \rho_{eg} \\ \rho_{ge} & \rho_{gg} \end{pmatrix}$$

$$\dot{\rho} = \begin{pmatrix} \dot{\rho}_{ee} & \dot{\rho}_{eg} \\ \dot{\rho}_{ge} & \dot{\rho}_{gg} \end{pmatrix}. \tag{3.9}$$

The term $\Gamma(t)\rho$ is the decay term, given by Eq. (3) of Ref. [24],

$$\Gamma\rho = \frac{\Gamma}{2}(\sigma_+\sigma_-\rho + \rho\sigma_+\sigma_-) - \Gamma\sigma_-\rho\sigma_+ \tag{3.10}$$

Written in terms of our Hamiltonian and the raising and lowering operators, the equation we get for the density matrix is

$$\begin{aligned}\dot{\rho} &= -i\omega(\sigma_+\sigma_-\rho - \rho\sigma_+\sigma_-) - i\frac{\Omega}{2}[(\sigma_+ + \sigma_-)\rho - \rho(\sigma_+ + \sigma_-)] \\ &+ \frac{\Gamma}{2}(2\sigma_-\rho\sigma_+ - \sigma_+\sigma_-\rho - \rho\sigma_+\sigma_-).\end{aligned} \tag{3.11}$$

If we insert Eq. (3.6) and Eq. (3.9) into this equation for the density matrix we get

$$\begin{pmatrix} \dot{\rho}_{ee} & \dot{\rho}_{eg} \\ \dot{\rho}_{ge} & \dot{\rho}_{gg} \end{pmatrix} = -i\omega \begin{pmatrix} 0 & \rho_{eg} \\ -\rho_{ge} & 0 \end{pmatrix} - \frac{i\Omega}{2} \begin{pmatrix} \rho_{ge} - \rho_{eg} & \rho_{gg} - \rho_{ee} \\ \rho_{ee} - \rho_{gg} & \rho_{eg} - \rho_{ge} \end{pmatrix} - \frac{\Gamma}{2} \begin{pmatrix} 2\rho_{ee} & \rho_{eg} \\ \rho_{ge} & -2\rho_{ee} \end{pmatrix} \tag{3.12}$$

In a 2-level system, the components of the Bloch vector are expressed by the Pauli matrices:

$$\sigma_x = \begin{pmatrix} 0 & 1 \\ 1 & 0 \end{pmatrix} \quad \sigma_y = \begin{pmatrix} 0 & -i \\ i & 0 \end{pmatrix} \quad \sigma_z = \begin{pmatrix} 1 & 0 \\ 0 & -1 \end{pmatrix}. \tag{3.13}$$

If we remember that the expectation value of an operator is the trace of the operator times the density matrix, we can show that

$$\langle\sigma_x\rangle = \mathrm{Tr}(\sigma_x\rho) = (\rho_{ge} + \rho_{eg})$$

$$\langle\sigma_y\rangle = \mathrm{Tr}(\sigma_y\rho) = i(\rho_{eg} - \rho_{ge})$$

$$\langle\sigma_z\rangle = \mathrm{Tr}(\sigma_z\rho) = (\rho_{ee} - \rho_{gg}). \tag{3.14}$$

We are concerned with how the internal state of the atom changes with time. We therefore want to find the time derivative of the expectation values of σ_x, σ_y, and σ_z, which are components of

the Bloch vector. Finding how they change in time tells us how the Bloch vector changes in time. Taking the derivative of Eq. (3.14) we get

$$
\begin{aligned}
\frac{d\langle\sigma_x\rangle}{dt} &= (\dot{\rho}_{ge} + \dot{\rho}_{eg}) \\
\frac{d\langle\sigma_y\rangle}{dt} &= i(\dot{\rho}_{eg} - \dot{\rho}_{ge}) \\
\frac{d\langle\sigma_z\rangle}{dt} &= (\dot{\rho}_{ee} - \dot{\rho}_{gg})
\end{aligned}
\tag{3.15}
$$

From Eq. (3.12) we have

$$
\begin{aligned}
\dot{\rho}_{ee} &= -\frac{i\Omega}{2}(\rho_{ge} - \rho_{eg}) - \Gamma\rho_{ee} \\
\dot{\rho}_{eg} &= -i\omega\rho_{eg} - \frac{i\Omega}{2}(\rho_{gg} - \rho_{ee}) - \frac{\Gamma}{2}\rho_{eg} \\
\dot{\rho}_{ge} &= i\omega\rho_{ge} - \frac{i\Omega}{2}(\rho_{ee} - \rho_{gg}) - \frac{\Gamma}{2}\rho_{ge} \\
\dot{\rho}_{gg} &= -\frac{i\Omega}{2}(\rho_{eg} - \rho_{ge}) + \Gamma\rho_{ee}.
\end{aligned}
\tag{3.16}
$$

Putting it all together, the equations of motion, written in terms of Pauli matrices, are

$$
\begin{aligned}
\frac{d\langle\sigma_z\rangle}{dt} &= \Omega\langle\sigma_y\rangle - \gamma(1 + \langle\sigma_z\rangle) \\
\frac{d\langle\sigma_y\rangle}{dt} &= \omega\langle\sigma_x\rangle - \Omega\langle\sigma_z\rangle - \frac{\gamma}{2}\langle\sigma_y\rangle, \\
\frac{d\langle\sigma_x\rangle}{dt} &= -\omega\langle\sigma_y\rangle - \frac{\gamma}{2}\langle\sigma_x\rangle.
\end{aligned}
\tag{3.17}
$$

The fluorescence signal $f(t)$ depends on time as

$$
f(t) = \frac{1}{2}[1 + \langle\sigma_z(t)\rangle].
\tag{3.18}
$$

We simulate decay from the excited state to the metastable dark $3d$ state by multiplying the total fluorescence rate by the branching ratio. This gives us the decay rate into the optically dark $3d\ ^2D_{3/2}$ state. We multiply this decay rate by the time step dt to find the probability that the ion
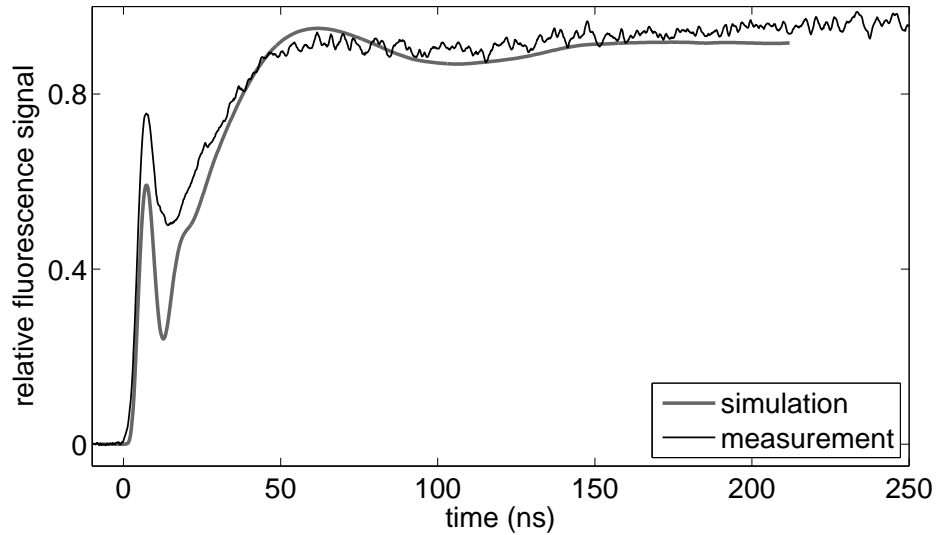
Figure 3.1 A comparison of the simulated fluorescence data (thick gray line) and the experimentally measured fluorescence (thin black line). Similar features are seen in both data sets, such as a heavily damped Rabi oscillation at early times, the DIH shoulder peak, and the broad background due to the plasma expansion. The density for these plots is $n_0 = 5(3) \times 10^{10}$ cm^{-3}.

has made a transition to this state. This probability is compared to a random number between 0 and 1. If the probability of decay is greater than this random number, the simulated ion transitions to the dark state and no longer fluoresces.

3.3   Comparison of simulated and experimental fluorescence data

Comparing the results of the simulation for a range of densities with experimental data shows good agreement, as seen in Fig. 3.1. Similar features in both signals are clearly distinguishable, such as a heavily damped Rabi oscillation at early times and the DIH shoulder, which will be discussed in greater detail in Sec. 4.1. Differences in the height of the signal can be attributed to inhomogeneities in the experimental setup. Since the simulated and experimental data agree well, we can use the simulation to obtain information about the plasma that would otherwise be difficult

to measure. Since we solve for the ion velocity at each time step we are able to extract the ion velocity distribution, which also allows us to find the time-evolving ion temperature at early times in the plasma evolution.

Chapter 4

Data and Discussion

The models described in Sec. 1.2.1 and Sec. 1.2.2 suggest that the time scale for DIH is insensitive to electron screening. If this were the case, we would expect the heating time to be the same across a range of electron temperatures. We can test this by going to colder electron temperatures and higher densities, which gives a smaller Debye length, corresponding to greater electron screening. The following sections detail a study of electron screening for a wider range of κ than previously studied.

4.1   Density and temperature scaling

Fluorescence measurements were made during the DIH phase to determine the time scale on which DIH occurred for a range of plasma densities and initial electron temperatures. Sample fluorescence data are shown in Fig. 4.1 for $T_e = 20$ K, $n_0 = 5 \times 10^{16}$ m^3, and a probe laser beam detuning of 90 MHz. At time $t = 0$ the plasma is generated, and the ground-state ions begin to interact with the probe laser beam and scatter photons. The sharp peak around 7 ns is a strongly damped Rabi oscillation. The second shoulder peak in the fluorescence signal, seen at about 70 ns, is the feature that we will refer to as the DIH peak, i.e. the time at which the fluorescence signal
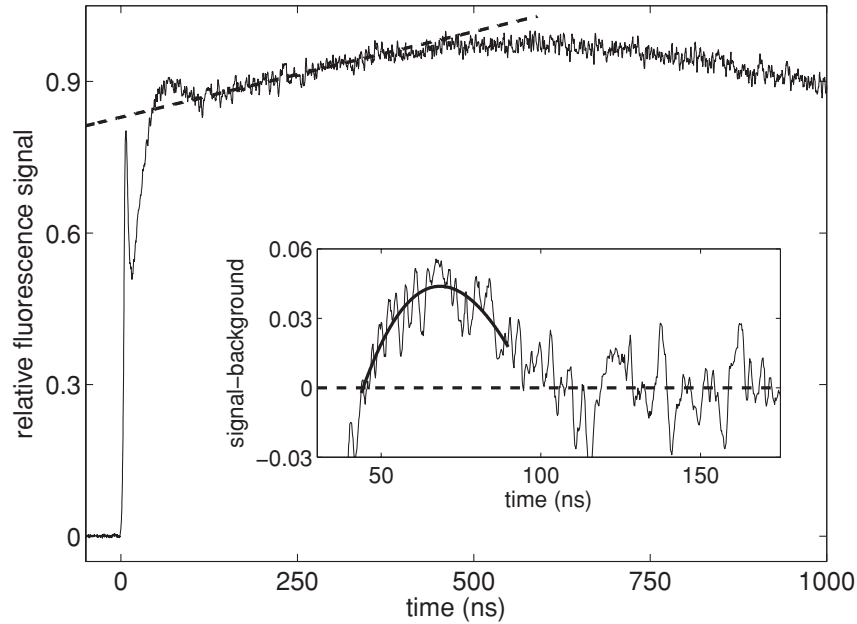
Figure 4.1 Typical fluorescence signal and analysis at $T_\mathrm{e} = 20$ K, $n_0 = 5 \times 10^{16}$ m^{-3}, $s_0 = 1.7$, and probe laser beam detuning of -90 MHz. A heavily damped Rabi oscillation appears at 7 ns. The shoulder peak at 70 ns is due to DIH broadening of the velocity distribution. The much broader peak near 600 ns is due to the accelerated expansion of the plasma. The dashed line is a linear fit to the background expansion. The inset shows the DIH peak with the background expansion subtracted. The background subtracted DIH peak is fit to a parabola, indicated by the heavy solid line, and the maximum of this fit is the characteristic DIH time t_0.

peaks due to DIH. This peak arises as the velocity distribution of the ions broadens due to DIH. Previous work has shown that, in the absence of electron screening, the DIH time is proportional to the inverse plasma frequency. A much broader peak occurs later, when the ion velocity distribution is further broadened by the outward radial acceleration of the expanding plasma and more ions are Doppler-shifted into resonance with the probe laser beam. The inset of Fig. 4.1 shows the DIH peak with the slope of the background expansion of the plasma subtracted off. The DIH peak is fit to a parabola, and the maximum of this parabolic fit is called t_0.

Data showing the temperature and density dependence of the DIH time t_0 is plotted in Fig. 4.2. As previously mentioned, past studies have shown that $t_0 \propto n^{-1/2}$ through the DIH time's rela-
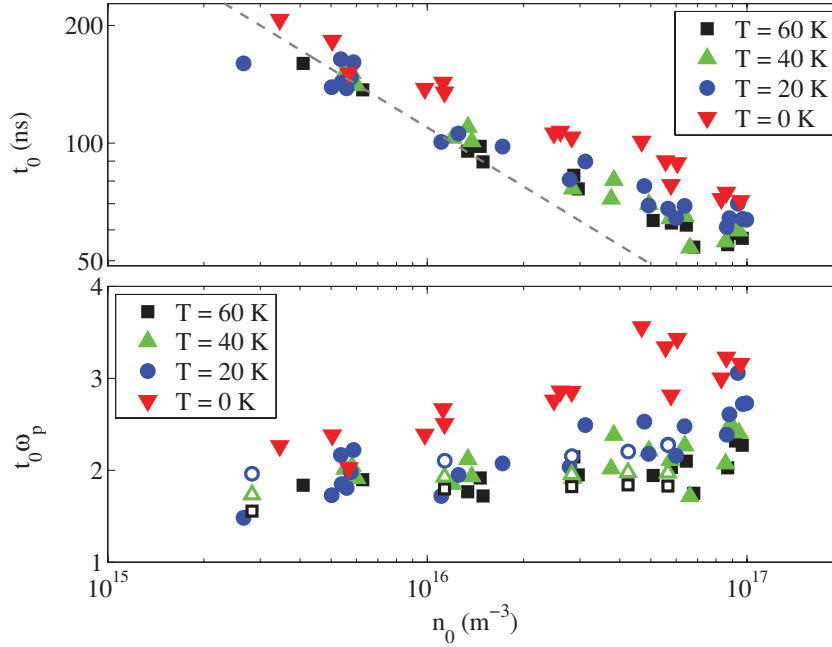
Figure 4.2 Experimental data. (Top) The time at which the DIH fluorescence peak occurs. The gray dashed line shows the expected time in the absence of screening effects. (Bottom) Scaled DIH peak time (data from the top panel) with t_0 corrected by Δt). Open symbols are from the simulation. This data would all fall on a flat line if there was no screening.

tionship to the inverse plasma frequency. The expected DIH time of this density dependence, in the absence of the electron screening, is plotted as the gray dashed line in the top panel of Fig. 4.2. We see that at low densities and electron temperatures much greater than the correlation temperature T_c (see Eq. (1.2)) that the $t_0 \propto n^{-1/2}$ relationship holds. However, as we decrease the screening length λ_D by increasing the density and bringing the electron temperature closer to T_c, we see that the time t_0 departs from the expected $n^{-1/2}$ scaling. The bottom panel of Fig. 4.2 shows the same effect more clearly, where the time has been scaled by the plasma frequency ω_p. In the absence of screening, we would expect all of the data to fall on the same horizontal line.

Comparing the experimental data with the simulation allows us to connect the DIH time found from our fluorescence measurements to the velocity distribution. We would expect t_0 to occur

at the same time that the rms velocity distribution reaches its first maximum. We find, however, that there is a small difference, Δt, that depends most strongly on density. We have applied this correction, which is $\leq 15\%$, in the bottom panel of Fig. 4.2. The data clearly shows in both panels that the DIH time deviates from the expected $n^{-1/2}$ dependence as the temperature decreases and the density increases. Further research was needed to determine whether this deviation was an effect of electron screening on the ion motion during DIH, or whether it was related to Δt. We also found a factor of 2 discrepancy between the experimental and simulated densities. As of yet we are not sure why this discrepancy arises, though we suspect it may have to do with how we measure the density experimentally. In the comparisons between experimental and simulated data, the densities of the experimental data have been multiplied by this factor of 2.

4.2 Detuning dependence of the fluorescence signal

In order to better understand the results outlined in Sec. 4.1 we made measurements of the fluorescence signal at different electron temperatures and at different probe laser beam detunings. Changing the frequency of the probe laser beam allows us to map out the velocity distribution, as explained in Sec. 2.2.2. Figure 4.3 shows fluorescence measurements from an ultracold plasma when the probe laser beam is detuned by 0, -70, and -140 MHz (0, -3.2, and -6.4 times the natural linewidth). As seen previously, plasma ions, initially all in the ground state, begin to scatter light from the 397 nm probe laser beam when the plasma is created (time $t = 0$), and the fluorescence signal rapidly rises during the first several ns. The ions are accelerated due to DIH, which broadens the velocity distribution. Depending on the probe laser beam detuning, this broadening affects the fluorescence signal differently.

When the probe laser beam is on resonance (black line in Fig. 4.3), the fluorescence signal falls rapidly between 25 and 100 ns. The DIH process is the dominant mechanism for broadening the
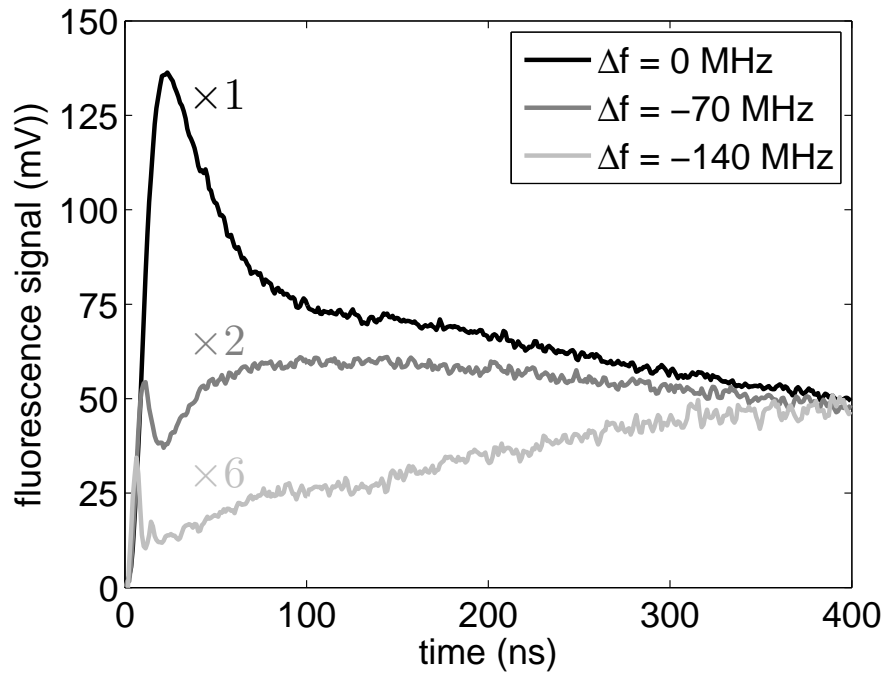
Figure 4.3 Fluorescence signals from an ultracold neutral calcium plasma. The density is $n_0 = 1 \times 10^{10}$ cm^{-3}, the intensity is $s_0 = 1.4$, and the probe laser beam frequency detunings are 0, -70, and -140 MHz. The -70 and -140 MHz data have been multiplied by 2 and 6 for clarity. Ground state ions begin to scatter light from the 397 nm probe laser beam and the signal rapidly increases during the first few ns. At non-zero probe laser beam detunings, a heavily damped Rabi oscillation appears in the signal. As the ion velocity distribution broadens due to DIH and plasma expansion, the fluorescence signals change. The fluorescence signal is a measure of the number of ions in the plasma that are Doppler shifted into resonance with the probe laser beam.

velocity distribution during this time. The signal level falls because fewer ions remain near zero velocity as time goes on. At later times, the plasma expansion becomes important. The plasma is not trapped in the MOT. Electron pressure that arises from the non-zero electron temperature accelerates the radial expansion and broadens the velocity distribution. The much slower decrease in fluorescence after 100 ns is due primarily to this radial acceleration of the plasma.

If we change the detuning of the probe laser beam, the fluorescence signal changes significantly. The medium gray line in Fig. 4.3 shows fluorescence measurements with the probe laser beam detuned -70 MHz (-3.2 linewidths). The first few ns of the fluorescence signals now show a heavily damped Rabi oscillation. The oscillation is damped out due to the spontaneous decay of the excited state and also by ion acceleration during the DIH phase. Ions with different velocities experience different Doppler-shifted detunings of the probe laser beam. This means that the Rabi oscillation frequency is different for ions with different velocities. The average of these different Rabi oscillation frequencies produces the narrower initial fluorescence peak near 10 ns.

When the probe laser beam is detuned from resonance, DIH-broadening and plasma expansion Doppler-shift ions into resonance with the probe laser beam. Initially there are no ions in resonance with the detuned probe laser beam. However DIH broadens the distribution causing a corresponding increase in the fluorescence signal. Notice that the -70 MHz data reaches a maximum around 100 ns, approximately equal to the time at which the slope in the 0 MHz detuning data changes. After this time, the -70 MHz signal decreases as the accelerated expansion continues to broaden the distribution so that the width exceeds the 70 MHz detuning and the fluorescence signal falls.

The light gray line in Fig. 4.3 shows the fluorescence signal when the probe laser beam is detuned by -140 MHz. The Rabi oscillations are still heavily damped. A few complete oscillation cycles can be seen at early times. The DIH broadening produces a small broad shoulder on the fluorescence data near 90 ns. The fluorescence signal continues to increase after this and reaches a maximum when the accelerated expansion has sufficiently broadened the velocity distribution. For

our plasma conditions at this detuning this occurs at 1.4 μs.

4.3 Extracting the rms velocity width

From fluorescence signals like the one shown in Fig. 4.3 we can extract the rms width of the velocity distribution as a function of time. As discussed in Ref. [5] the fluorescence lineshape is a Voigt profile. However, when the Gaussian width significantly exceeds the Lorentzian width, the lineshape is almost perfectly Gaussian. When the ion temperature equals T_c, the thermal velocity is $\sqrt{k_B T_c/m_i} = 28$ m/s. The natural width of the Ca^+ transition is 22 MHz. The ion velocity that produces a Doppler shift equal to this width is 8.7 m/s. Fitting the velocity distribution to a Gaussian instead of a Voigt profile somewhat overestimates the real ion temperature. However, changes in the width of the distribution can be readily measured.

As a model, we take the velocity distribution to be Gaussian of the form

$$F(v) = F_0^v \exp(-v^2/2v_{rms}^2), \tag{4.1}$$

where $v_{rms} = \sqrt{k_B T_i/m_i}$ is the rms thermal velocity and F_0^v is a normalization constant for the distribution. We don't have access directly to the velocity distribution. However the velocity and the frequency are related to each other through the Doppler shift, with $v = \lambda f$ where λ is the transition wavelength in vacuum and f is the transition frequency. Therefore the velocity distribution can be mapped into a transition frequency distribution as

$$F(f) = F_0^f \exp(-f^2/2f_{rms}^2), \tag{4.2}$$

where $f_{rms} = v_{rms}/\lambda$.

We can look at our fluorescence data measurements at different detunings at one particular time t_i. These data form a set,

$$y_i(f,t_i) = c_1(t_i)\exp(-f^2/2c_2^2(t_i)), \tag{4.3}$$

where $c_1(t_i)$ and $c_2(t_i)$ are parameters that describe the frequency (and hence velocity) distribution. The logarithm of Eq. (4.3) is written

$$\ln[y_i(f,t_i)] = \ln[c_1(t_i)] - \frac{f^2}{2c_2^2(t_i)}. \tag{4.4}$$

This gives a quadratic relation between the log of the fluorescence signal and the width of the frequency distribution. In our analysis we fit the log of the fluorescence signal vs. frequency to the equation

$$\ln[y_i(f,t_i)] = a_1(t_i) - a_2(t_i) f^2 \tag{4.5}$$

using a least-squares method. The fit parameter $2a_2(t_i) = [c_2(t_i)]^{-2}$ is used to extract $c_2(t_i)$, the time-evolving rms width of the frequency distribution. The frequency width is then used to determine the rms velocity width, $v_{rms}(t_i) = \lambda c_2(t_i)$. The results of this analysis are shown in Fig. 4.4 for two different initial electron temperatures.

During the first 15 ns of the fluorescence signals, Rabi oscillations make it difficult to extract a meaningful velocity width. After these oscillations damp out, the rms velocity appears to be more reliable. We can verify that the minimum width of the distribution corresponds to the correlation temperature, Eq. (1.2). The rms velocity at the correlation temperature is 28 m/s at our density of $n_0 = 1.0 \times 10^{10}$ cm^{-3}. The minimum width of our extracted velocity distribution of approximately 20 m/s agrees with this number.

At late times in the plasma expansion, the radial acceleration approaches zero and the expansion velocity approaches a constant value. In our measurements of the $T_e = 60$ K plasma, the width of the velocity distribution asymptotically approaches the value of 115 m/s. This is a close match to the expected value of $\sqrt{k_B T_e/m_i} = 111$ m/s.

The velocity distribution shows a small oscillation at early times. This oscillation is shown in Fig. 4.5 and is similar to what has been reported in the literature (for example [5, 6]). The oscillation occurs because the ions are initially at rest and all begin to move at the same time. They
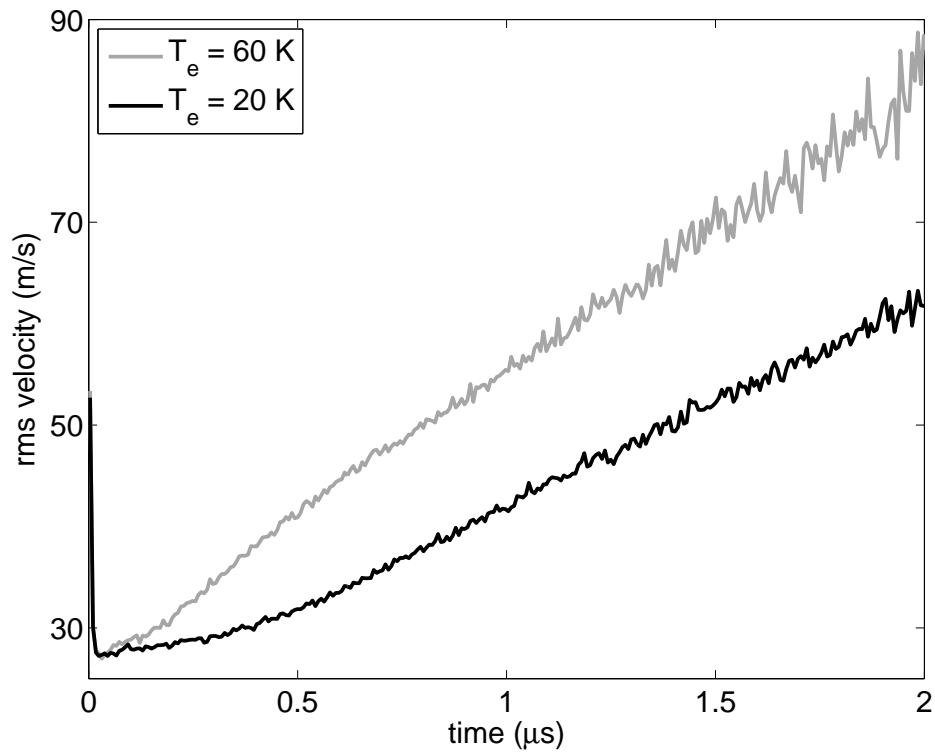
Figure 4.4 The rms width of the ion velocity distribution as a function of time in an ultracold calcium plasma. This data is extracted using a Gaussian fit as described in the text. At early times this fit overestimates the width. However it reproduces changes in the distribution and that is the main objective in this graph.
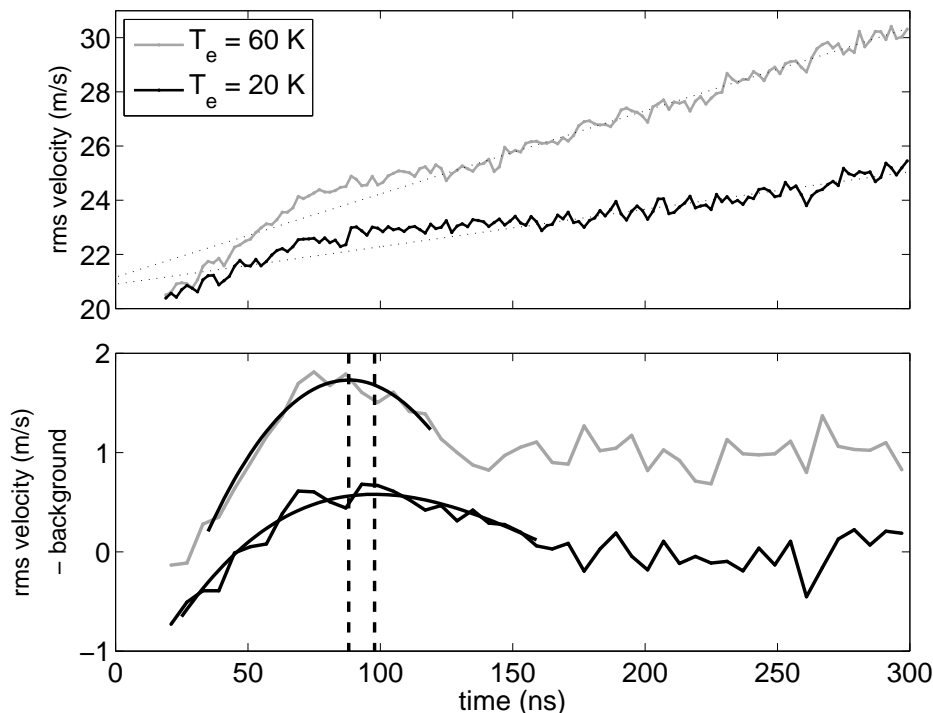
Figure 4.5 Top (panel): Velocity distribution at early times. Data for this plot was extracted from a subset of the fluorescence data, with probe laser detunings of 140 MHz and smaller, for initial electron temperatures $T_e = 20$ K and $T_e = 60$ K, and an initial plasma density of $n_0 = 1.0 \times 10^{10}$ cm^{-3}. An oscillation in the velocity distribution is visible above the background expansion, represented by the dotted line. Bottom (panel): The data in the top panel with the background expansion subtracted off. A third-order polynomial fit to the early time data is shown by the smooth solid black line. The maxima of these polynomial fits are shown by the vertical dashed lines. The $T_e = 60$ K data is offset vertically for clarity. As the electron temperature decreases, the DIH peak broadens and moves to later times.

move to minimize their electric potential energy. Each ion finds itself in a local potential well and the shape of that well depends on the positions of neighboring ions and electrons. Variations in these local potential wells cause the ion motion, which starts coherently, to dephase as the plasma relaxes. This dephasing time is comparable to the oscillation period [18], and only a partial cycle is observed in our data.

The top panel of Fig. 4.5 shows the width of the velocity distribution at early times. As men-

tioned previously, the width determined from the first 15 ns of fluorescence signal oscillates wildly because of Rabi oscillations in the data. Therefore Fig. 4.5 shows data only from 15 to 300 ns. The dotted line in the top panel of Fig. 4.5 is a fit that represents the plasma expansion.

The bottom panel of Fig. 4.5 shows the width of the velocity distribution with the background expansion subtracted off. A vertical offset is included to distinguish between the data sets at the two different initial electron temperatures. A third-order polynomial is fit to the data near 100 ns. From the fits we are able to extract the time at which the DIH process broadens the distribution to its maximum value, which is equivalent to what we have previously called the DIH peak. The times at which the DIH peaks occur are indicated by the dashed vertical lines. For an initial electron temperature of $T_e = 60$ K this DIH peak occurs at 88 ns. For an initial electron temperature of $T_e = 20$ K the peak occurs at 98 ns. For the lower temperature plasma the DIH peak is also broader, indicating that the equilibration rate is slower. These two effects are due to electron screening.

The effects of electron screening described by Eq. (1.10) should appear in the data plotted in the bottom panel of Fig. 4.5. As the initial electron temperature decreases from 60 K to 20 K, the value of κ increases from 0.54 to 0.93. This reduces the initial acceleration in Eq. (1.10) by 2.5%. In the bottom panel of Fig. 4.5 the characteristic DIH time, the time at which v_{rms} reaches its local maximum due to DIH, increases by $[(98\,\mathrm{ns}/88\,\mathrm{ns}) - 1] \times 100 = 11\%$. This indicates a reduction in the average acceleration by approximately the same amount.

It is perhaps not surprising that the observed acceleration is smaller than in Eq. (1.10) because we have truncated the original expression for the ion temperature. The scaled time at 88 ns is 1.8, suggesting that higher order terms in Eq. (1.8) are important. In particular we note that the coefficient of the t^4 term is negative [6]. This would reduce the ion acceleration as the plasma evolves. A more detailed study of this effect is needed.

When $\kappa = 0.93$, the number of particles per Debye sphere is $n\lambda_D^3 = 3/4\pi\kappa^3 = 0.3$. In this limit the concept of Debye shielding is perhaps questionable, although it has been pointed

out that the electrons move rapidly on the time scale of the ion motion and this may make Debye shielding a reasonable concept in this regime. We also note that recombination and electron-Rydberg scattering can increase the electron temperature and give a smaller value of κ. However these effects are not expected to be important at a density of $n_0 = 10^{10}$ cm^{-3} and an initial $T_e = 20$ K on the 100 ns time scale.

Chapter 5

Conclusions and future work

Initial data shows that electron screening plays a more significant role in the equilibration process of ions in ultracold neutral plasmas than previously measured or calculated. We observed that at higher densities and lower electron temperatures, which correspond to smaller Debye lengths and therefore greater electron screening, the characteristic DIH time was extended and that the rate of equilibration slowed. We would also expect to see a lower ion equilibration temperature as a result of electron screening, however the data quality was such that we did not observe these effects. Efforts are underway to improve the data quality, which would allow us to use a Voigt profile rather than a Gaussian fit to extract the rms velocity width. Fitting the frequency distribution described in Sec. 4.3 to a Voigt profile will give us a more accurate representation of the ion velocity distribution and therefore the ion temperature as well.

As the number of particles per Debye sphere decreases and approaches values less than one, the models we use to describe electron screening are called into question. Since Debye shielding occurs on the length scale of the Debye length, when we shorten the Debye length we also reduce the probability of finding a charge within a volume λ_{D}^3. The physics used to describe interactions between ions in plasmas is not valid if we must take into consideration the strong, short-range interactions that become important when $n\lambda_{\mathrm{D}}^3 \leq 1$ [25]. We can explore this regime by looking at

high-density and very low-temperature plasmas. In this regime we must also consider a possible lowest limit on the electron screening length due to electron heating. Similar to ions, electrons go through an equilibration process at early times. Strong coupling of electrons is limited by DIH of the electrons to $\Gamma_e \sim 1$ and by other heating mechanisms, such as three-body recombination and electron-Rydberg scattering, to $\Gamma_e \leq 0.2$. At lower initial electron temperatures, these heating mechanisms become important at early times as well as later. Future studies include exploring electron screening, DIH, and other equilibration processes in systems in which these heating mechanisms are important at early times and in systems in which both the electrons and the ions are strongly coupled.

Although the data shows that electron screening extends the DIH time and we expect that it should also reduce the ion equilibration temperature, it is not clear that electron screening will allows us to achieve a higher Γ. This is because electron screening softens the Coulomb potential between ions. Since Γ is directly proportional to the nearest-neighbor Coulomb energy, decreasing this potential via electron screening also reduces Γ.

Efforts are underway that will allow us to achieve higher values of Γ by promoting the plasma ions to higher ionization states at the conclusion of the DIH phase. Such an experiment was proposed and simulations were carried out in Ref. [26]. Previously measured ion strong coupling parameter values have been on the order of of $\Gamma \sim 4$ in our Ca^+ plasmas. If these ions are ionized again to form Ca^{2+}, higher values of Γ could be achieved. Three-body recombination, electron-Rydberg scattering, collisional heating could then be studied in a neutral system where Γ is in a new range of values.

By varying the time at which the $Ca^+ \rightarrow Ca^{2+}$ transition occurs, a wide range of Γ values could be realized, as suggested in Ref. [26]. For example if the transition to the second ionization stage occurs coincident with the first ionization, DIH will limit Γ to values near 1. However if the transition to the second ionization stage occurs at 100 ns, for example, after the DIH associated

with the first ionization has damped out, simulations suggest that Γ will increase perhaps by a factor of 4. It is therefore advantageous for us to continue to investigate the time scale over which DIH occurs and the effects of electron screening on the characteristic DIH time, as characterizing these effects will allow us to more effectively explore this new realm of study.

Bibliography

[1] N. C. Woolsey, D. Riley, and E. Nardi, "Kilovolt x-ray scattering from a plasma," Rev. Sci. Instrum. **69,** 418 (1998).

[2] T. B. Mitchell, J. J. Bollinger, X. Huang, W. M. Itano, and D. H. Dubin, "Direct Observations of Structural Phases in Crystallized Ion Plasmas," Physics of Plasmas **6,** 1751 – 1758 (1999).

[3] J. H. Chu and I. Lin, "Direct observation of Coulomb crystals and liquids in strongly coupled rf dusty plasmas," Phys. Rev. Lett. **72,** 4009–4012 (1994).

[4] H. M. Van Horn, "Dense Astrophysical Plasmas," Science **252,** 384–389 (1991).

[5] Y. C. Chen, C. E. Simien, S. Laha, P. Gupta, Y. N. Martinez, P. G. Mickelson, S. B. Nagel, and T. C. Killian, "Electron Screening and Kinetic-Energy Oscillations in a Strongly Coupled Plasma," Phys. Rev. Lett. **93,** 265003 (2004).

[6] M. S. Murillo, "Ultrafast Dynamics of Strongly Coupled Plasmas," Phys. Rev. Lett. **96,** 165001 (2006).

[7] S. Laha, Y. C. Chen, P. Gupta, C. E. Simien, Y. N. Martinez, P. G. Mickelson, S. B. Nagel, and T. C. Killian, "Kinetic energy oscillations in annular regions of ultracold neutral plasmas," Eur. Phys. J. D pp. 51–56 (2006).

[8] J. Castro, P. McQuillen, H. Gao, and T. C. Killian, "The role of collisions and strong coupling in ultracold plasmas," Journal of Physics: Conference Series **194,** 012065 (2009).

[9] T. C. Killian, "Ultracold Neutral Plasmas," Science **316,** 705 – 708 (2007).

[10] C. E. Simien, Y. C. Chen, P. Gupta, S. Laha, Y. N. Martinez, P. G. Mickelson, S. B. Nagel, and T. C. Killian, "Using Absorption Imaging to Study Ion Dynamics in an Ultracold Neutral Plasma," Phys. Rev. Lett. **92,** 143001 (2004).

[11] E. A. Cummings, J. E. Daily, D. S. Durfee, and S. D. Bergeson, "Fluorescence measurements of expanding strongly coupled neutral plasmas," Phys. Rev. Lett. **95,** 235001 (2005).

[12] S. G. Kuzmin and T. M. O'Neil, "Numerical Simulation of Ultracold Plasmas: How Rapid Intrinsic Heating Limits the Development of Correlation," Phys. Rev. Lett. **88,** 065003 (2002).

[13] T. C. Killian, S. Kulin, S. D. Bergeson, L. A. Orozco, C. Orzel, and S. L. Rolston, "Creation of an Ultracold Neutral Plasma," Phys. Rev. Lett. **83,** 4776–4779 (1999).

[14] S. Kulin, T. C. Killian, S. D. Bergeson, and S. L. Rolston, "Plasma Oscillations and Expansion of an Ultracold Neutral Plasma," Phys. Rev. Lett. **85,** 318–321 (2000).

[15] T. C. Killian, M. J. Lim, S. Kulin, R. Dumke, S. D. Bergeson, and S. L. Rolston, "Formation of Rydberg Atoms in an Expanding Ultracold Neutral Plasma," Phys. Rev. Lett. **86,** 3759–3762 (2001).

[16] E. A. Cummings, J. E. Daily, D. S. Durfee, and S. D. Bergeson, "Ultracold neutral plasma expansion in two dimensions," Physics of Plasmas **12,** 3501 (2005).

[17] J. P. Morrison, C. J. Rennick, and E. R. Grant, "Very slow expansion of an ultracold plasma formed in a seeded supersonic molecular beam of NO," Phys. Rev. A **79,** 062706 (2009).

[18] T. Killian, T. Pattard, T. Pohl, and J. Rost, "Ultracold neutral plasmas," Physics Reports **449,** 77 – 130 (2007).

[19] F. Robicheaux and J. D. Hanson, "Simulation of the Expansion of an Ultracold Neutral Plasma," Phys. Rev. Lett. **88,** 055002 (2002).

[20] P. Gupta, S. Laha, C. E. Simien, H. Gao, J. Castro, T. C. Killian, and T. Pohl, "Electron-temperature evolution in expanding ultracold neutral plasmas," Phys. Rev. Lett. **99,** 075005 (2007).

[21] S. L. Rolston, "Ultracold neutral plasmas," Physics **1,** 2–2–1 (2008).

[22] S. D. Bergeson, A. Denning, M. Lyon, and F. Robicheaux, "Density and temperature scaling of disorder-induced heating in ultracold plasmas," Phys. Rev. A **83,** 023409 (2011).

[23] M. S. Murillo, "Using Fermi Statistics to Create Strongly Coupled Ion Plasmas in Atom Traps," Phys. Rev. Lett. **87,** 115003 (2001).

[24] K. Mølmer, Y. Castin, and J. Dalibard, "Monte Carlo wave-function method in quantum optics," J. Opt. Soc. Am. B **10,** 524–538 (1993).

[25] T. C. Killian and S. L. Rolston, "Ultracold neutral plasmas," Physics Today **63,** 46–51 (2010).

[26] M. S. Murillo, "Ultrafast dynamics of neutral, ultracold plasmas," Physics of Plasmas **14,** 055702 (2007).